Aalborg Universitet

AALBORG UNIVERSITY
DENMARK

Nonlinear Stability Analysis for Three-phase Grid-connected PV Generators

Wei, Wei; Xia, Yanghong; Blaabjerg, Frede

Published in:
I E E E Journal of Emerging and Selected Topics in Power Electronics

DOI (link to publication from Publisher):
10.1109/JESTPE.2019.2939379

Publication date:
2020

Document Version
Accepted author manuscript, peer reviewed version

Link to publication from Aalborg University

Citation for published version (APA):
Wei, W., Xia, Y., & Blaabjerg, F. (Accepted/In press). Nonlinear Stability Analysis for Three-phase Grid-connected PV Generators. *I E E E Journal of Emerging and Selected Topics in Power Electronics*, *8*(4), 3487-3501. [8823866]. https://doi.org/10.1109/JESTPE.2019.2939379

General rights
Copyright and moral rights for the publications made accessible in the public portal are retained by the authors and/or other copyright owners and it is a condition of accessing publications that users recognise and abide by the legal requirements associated with these rights.

? Users may download and print one copy of any publication from the public portal for the purpose of private study or research.
? You may not further distribute the material or use it for any profit-making activity or commercial gain
? You may freely distribute the URL identifying the publication in the public portal ?

Take down policy
If you believe that this document breaches copyright please contact us at vbn@aub.aau.dk providing details, and we will remove access to the work immediately and investigate your claim.

Downloaded from vbn.aau.dk on: December 25, 2020

This article has been accepted for publication in a future issue of this journal, but has not been fully edited. Content may change prior to final publication. Citation information: DOI 10.1109/JESTPE.2019.2939379, IEEE Journal of Emerging and Selected Topics in Power Electronics

Nonlinear Stability Analysis for Three-phase Grid-connected PV Generators

Wei Wei, Yanghong Xia, *Member, IEEE* and Frede Blaabjerg, *Fellow, IEEE*

***Abstract*—Numerous emerging oscillatory stability issues have recently arisen as renewable energy sources are integrated into the power system. Some of the existing literature attempts to explain these issues through corresponding simplification, which usually omits the influence of the nonlinear discontinuous elements in the system. Hence, the obtained results are incomplete. To fill in this gap, this paper proposes a stability analysis method based on the describing function (DF) method to explore the influence of nonlinear discontinuous elements in the system. Without loss of generality, taking the three-phase grid-connected photovoltaic (PV) generator as the research object, the perturbation and observation (P&O)-based power control, which is a typical nonlinear discontinuous element, was carefully studied. First, the complete mathematical model of the three-phase grid-connected PV generator was established, including the outermost P&O-based power control. Then, according to the DF method, the stability of the PV generator was analyzed, and the related influence factors were studied in detail. It was found that the nonlinear discontinuous P&O-based power control has substantial influence on the stability of the PV generator and can result in the oscillation. At the same time, the DF method and the conventional method were compared, which shows that the proposed DF method can enhance the accuracy of the stability assessment. Especially regarding critical stability, the oscillation magnitude and frequency can be calculated accurately. All the theoretical analyses were verified by the real-time hardware-in-loop (HIL) tests.**

***Index Terms*—PV generators, nonlinearity, stability analysis, describing function method.**

I. Introduction

IN recent years, with the increase in the penetration of renewable energy sources (RESs), more and more accidents such as the sub- or super-synchronous oscillations at a centralized wind farm [1]-[4], low-frequency oscillations caused by distributed photovoltaic (PV) generators [5]-[7], and high-frequency harmonics in islanded microgrids [8]-[9] are reported when RESs are integrated into the power system. These stability issues will cause the breakdown of RESs and endanger the normal operation of the power system, which will greatly influence the efficient and reliable utilization of RESs. Therefore, the stability analysis of RESs integrated into the power system has attracted significant attention.

To propose better solutions, the mechanism of the instability is extensively researched when RESs are integrated into the power system. The analysis methods and the possible main influence factors from the existing literature can be summarized briefly, as shown in Fig. 1. Through the corresponding simplification, the RES generators can be processed into a purely linear system. Then, according to the mature frequency-domain and time-domain methods, the related influence factors can be analyzed. Due to the different simplifications and different assumptions, the obtained results are varied, and there is no definitive consensus that can explain the instability phenomena well. Hence, the exploration of the mechanism of the instability when the RESs are integrated into the power system is still an open problem.

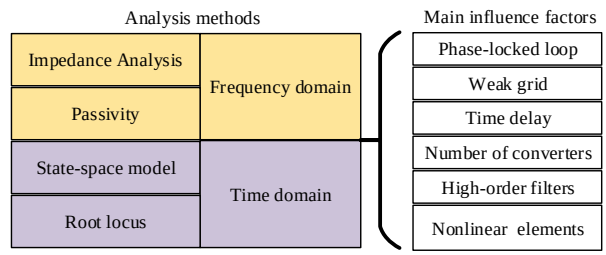

Fig.1. Brief summary for the existing literature.

The centralized large-scale wind farms and PV plants are prone to generate oscillatory problems when they are connected to a weak grid. Some scholars think that the phase-locked loop (PLL) used for the synchronization may cause the instability issues under the circumstance of a weak grid [10]-[16]. In these papers: a) The filters selected are the simple first-order *L*-type filters, which avoid the possible influence of the high-order filters; and b) The dynamics of the RESs, such as PV panels and the outermost power control, are completely omitted.

Since the PLL is inherently nonlinear, the conventional linear PLL models cannot capture its low-frequency dynamics well. Hence, a quasi-static large-signal model of the PLL is proposed to analyze its large-signal stability in [10]. The proposed model can accurately predict that unstable low-frequency (approximately 5-10 Hz) nonlinear oscillations will occur if a stiff grid changes into a weak grid. However, the established complicated nonlinear model is not suitable for the control system synthesis, especially for the multi-machine system. To accommodate more comprehensive applications, the small-signal impedance of grid-connected inverters is established based on the *dq* synchronous reference frame in [11]. The *q*–*q* channel impedance behaves as a negative

This work is supported in part by the National Key R&D Program of China (2017YFB0902002), in part by the Science and Technology Project of State Grid Corporation of China (SGXJ0000KXJS1700841). (*Corresponding author: Yanghong Xia*)

W. Wei and Y. Xia are with the College of Electrical Engineering, Zhejiang University, Hangzhou, 310027, China. (e-mail: royxiayh@126.com; wwei@zju.edu.cn).

F. Blaabjerg is with the Department of Energy Technology, Aalborg University, 9220 Aalborg, Denmark (e-mail: fbl@et.aau.dk).

2168-6777 (c) 2019 IEEE. Personal use is permitted, but republication/redistribution requires IEEE permission. See http://www.ieee.org/publications_standards/publications/rights/index.html for more information.

This article has been accepted for publication in a future issue of this journal, but has not been fully edited. Content may change prior to final publication. Citation information: DOI 10.1109/JESTPE.2019.2939379, IEEE Journal of Emerging and Selected Topics in Power Electronics

incremental resistor, which will cause instability when inverters are connected to the weak grid. Inspired by this finding, based on the impedance matching criteria, an impedance controller is proposed in [12] to reshape the *q*-*q* impedance into a positive resistance in the low-frequency band. Then, the stable margin of the grid-connected inverters can be enhanced. Based on the impedance analysis, the sub- and super-synchronous interactions between STATCOMs and weak ac/dc transmissions with series compensations are studied in [13], and the study concludes that the risk of oscillation could be decreased by increasing the strength of the ac grid. To improve the accuracy of the stability analysis, the dynamics of the capacitor on the dc side are modeled in [14]-[16]. That is, the dc side is no longer viewed as an ideal dc voltage source. In [14], the detailed model of the grid-connected converter is established, including the PLL dynamics, ac side dynamics and dc side dynamics. Through the root locus analysis, the unstable mechanism in the very weak grid condition is explained, and a robust vector control method is proposed. In some practical applications, the grid-connected converters need to provide the ac bus voltage support for the weak grid. The detailed model of this kind of grid-connected converter is established in [15]. Based on the model, the influence of grid strengths, PLL bandwidths and operation points on the system stability are carefully analyzed through the root locus analysis. Furthermore, the influence of the ac bus voltage control on the dc bus voltage stability is studied in [16], in which some physical insights such as damping and restoring components are given based on the state-space model. The presented results show that the PLL and ac-bus voltage control can impact active power, which further impacts the stability of the dc-bus voltage control.

In addition, some scholars also think that the high-order filters, namely, *LCL* filters account for the instability issues [17]-[22]. In these papers: a) The grid is stiff, and the dynamics of PLL can be ignored; and b) The dynamics of the RESs such as PV panels and the outermost power control are completely omitted as well.

Tang *et al.* [17] investigate the inherent damping characteristics of *LCL* filters for grid-connected converters. When the converter-side currents are used as feedback signals, there would be an inherent damping term embedded in the control loop, which can enhance the stability of the system. In [18], the influence of *LCL* filters is further studied with consideration of the time delay of the digital controller, showing that this influence factor easily results in the current regulation being susceptible to weak grid conditions. Then, an improved capacitor voltage feedforward control with full delay compensation is proposed to overcome the influence of the grid impedance and to provide a high-harmonic rejection capability without using additional harmonic compensators. To suppress the resonance of *LCL* filters, some active damping methods are used to attenuate the resonant behavior effectively. The effects of active damping on the output impedance of grid-connected converters are analyzed in [19]. Based on the impedance analysis, the improper active damping is shown to lead to harmonic instability. In [20], a systematic methodology for the design and tuning of the current and active damping controllers in *LCL* grid-connected converters is proposed through the combination of the impedance and root-locus analysis. The whole design objective is to minimize the current loop dominant time constant, which could minimize harmonic interactions around the resonance frequency. Taking both the influence of *LCL* filters and the PLL into consideration, Zhou *et al.* [21] propose that when the *LCL*-type grid-connected converters are attached to the weak grid, current control interacts with PLL via the voltage of the point of common coupling. Consequently, the PLL dynamic might deteriorate the grid current control and even result in system instability. Then, they suggest that through optimizing parameters, the negative effect of the PLL on current control can be reduced effectively. Considering the dynamics of PV panels, the stability of *LCL*-filtered PV generators is analyzed in [22]. It is revealed that the grid impedance has different influence on the system high-frequency and low-frequency stability.

In the recent reports, power oscillation often occurs among the large-scale distributed RES generators [23]-[26], where the number of RES generators obviously influences the oscillation modes. In [23], a unified *dq*-frame impedance network model is presented, through which different converters and traditional generators/HVDCs can all be incorporated to form a frequency-domain model. Based on the impedance analysis, the stability of the large system containing multiple converters is studied, and the authors conclude that the increasing number of RES generators will result in lower frequency and higher magnitude of the oscillations. The impedance analysis is based mainly on the magnitude of the impedance to evaluate the stability of the system. From the point of the phase of the impedance, the passivity-based method is another way to analyze the system stability. Compared to the impedance analysis that needs both the source and load information, the passivity-based method is more self-disciplined. If the components no matter the source or the load meet the passivity, both their parallel and feedback connection meet the passivity as well. That is, the corresponding stability can be ensured. Hence, the passivity-based method is more suitable for analysis with multiple converters. Harnefors *et al.* [24] present an overview of the passivity-based stability assessment for the grid-connected voltage-source converters based on the input admittance of the converters. In [25], based on the frequency-domain passivity theory, the harmonic stability of multi-paralleled *LCL*-type grid-connected converters is studied, and a corresponding damping injection strategy is designed to enhance the stability of the multi-machine system. In [26], the damping injection strategy in [25] is modified, and an extra series *LC*-filtered active damper is connected in shunt with the grid-connected converter to facilitate the passivity enhancement.

The power electronic devices inevitably have nonlinear elements. To study their influence, some advanced modeling methods have been developed [27]-[31]. In [27], the accuracy of the state-space average model is found to be questionable when the control-loop bandwidth is close to the switching frequency. For more accurate results, the harmonic linearization approach is used to establish the models of buck

2168-6777 (c) 2019 IEEE. Personal use is permitted, but republication/redistribution requires IEEE permission. See http://www.ieee.org/publications_standards/publications/rights/index.html for more information.

This article has been accepted for publication in a future issue of this journal, but has not been fully edited. Content may change prior to final publication. Citation information: DOI 10.1109/JESTPE.2019.2939379, IEEE Journal of Emerging and Selected Topics in Power Electronics

and multiphase buck converters. Then, their high-frequency behavior, especially the sideband effect, can be investigated accurately. For describing the switching behavior of diodes, Sun *et al.* [28] adopt the harmonic linearization modeling method to calculate the small-signal input impedance of line-frequency rectifiers. In [29], this method is extended to the multi-pulse rectifiers, where the modeling processes are introduced in detail. Furthermore, for the three-phase voltage-source converters, the decoupled positive-sequence and negative-sequence impedances are established directly in the phase domain through the harmonic linearization approach [30]. To overcome the time-varying characteristics of the single-phase system, the 2-D source and load impedances are determined through the dynamic phasor approach in [31]. These modeling methods can only deal with the situation where the relationship between the input signals and output signals of the nonlinear elements is not influenced by the amplitude of input signals, namely, $\hat{Y}(j\omega) = G(j\omega) \cdot \hat{X}(j\omega)$. If the relationship between the input signals and output signals of the nonlinear elements is related to the amplitude of input signals, namely,$\hat{Y}(j\omega) = G(j\omega, |\hat{X}(j\omega)|) \cdot \hat{X}(j\omega)$, then these modeling methods are not proper anymore.

In conclusion, the theoretical basis of the aforementioned methods relies mainly on the purely linear system theory, which will meet several challenges. First, through the small-signal modeling, the nonlinear but continuous elements can be considered. However, some nonlinear and discontinuous elements that are sensitive to the amplitude of the input signals, such as the widely used perturbation and observation (P&O)-based power control are completely ignored, because the relationship between the input signals and output signals is related to the amplitude. The whole system cannot be transformed into a purely linear system, so the well-developed analysis methods such as root locus analysis, Bode diagram analysis, etc., are not applicable anymore. Therefore, the accuracy of results obtained through these methods is challenged.

Second, for the purely linear system, the requirement of critical stability, i.e., persistent oscillation, is very strict. From the point of the Nyquist criterion, the Nyquist curve of the system must cross the point (-1, *j*0), which is the unique point in the whole *s* plane. Therefore, using linear system theory to analyze power oscillation instability issues is not suitable, since the strict oscillation criterion is difficult to find. Although the stable margin can be used to perfect the theory [32]-[35], some limitations still exist: 1) The stable margin is suitable only for the minimum phase system. For the non-minimum phase system, the stable margin is not suitable anymore; 2) The information about the oscillation is insufficient. Especially, the oscillation magnitude cannot be obtained, which results in the inability to conduct some quantitative analyses; and 3) Using the stable margin to assess the stability of the system, especially for the critical stability, is strongly dependent on the posteriori information, which can hardly provide prediction. That is, for a system, the stable margin is given, but it is difficult to say that the system is stable/critically stable or not, which must be further verified by the simulations or experiments.

To overcome the above disadvantages of the conventional stability analysis methods, this paper adopts the describing function (DF) method to analyze the stability of grid-connected RES generators with consideration of the complete control links. Compared to the small-signal modeling that is the time-domain approximation, the DF method is the frequency-domain approximation, and the nonlinear discontinuous elements can be considered. Without loss of generality, the three-phase grid-connected PV generator is chosen as the research object, for which the related research methods can be generalized to wind turbines and other RES generators. First, the complete mathematical model of the PV generator is established, which includes the nonlinear discontinuous P&O-based power control and the dynamics of the PV panel itself. Then, an overview of the DF method is presented, and the stability analysis is conducted. Being different from the conventional stability analysis method, the proposed DF method-based stability analysis includes the complete information for the system. Then, the critically stable criterion can be very accurate, and the oscillation can be analyzed quantitatively, where the oscillation frequency and magnitude can be calculated accurately. On this basis, the related influence factors including the operation points, filters, control bandwidth, etc., are carefully analyzed. It is found that the nonlinear discontinuous P&O-based power control has great influence on the stability of the PV generator and can result in the oscillation even under the stiff-grid condition. At the same time, the DF method and the conventional method are compared, which shows that the proposed DF method can enhance the accuracy of the stability assessment effectively. All the theoretical analyses are verified by the real-time HIL tests mainly composed of the RTLAB and TMS320F28335 DSPs.

The remainder of this paper is organized as follows. In Section Ⅱ, the detailed model of the three-phase grid-connected PV generator is derived. In Section Ⅲ, the DF method is introduced, and the stability analysis is conducted. The validity of the theoretical analyses is demonstrated through HIL tests in Section Ⅳ. Finally, the conclusions are drawn in Section Ⅴ.

II. Modeling of Three-phase Grid-connected PV Generators

In this section, the detailed and complete mathematical model of the three-phase grid-connected PV generator is derived. As shown in Fig. 2(a), the output current and voltage of the PV panel are i_{pv} and v_{pv}, respectively, and the capacitance of the capacitor across the PV panel is *C*. The PV generator is connected to the stiff grid through the *L*-type filter *L*, and its output currents are $i_{a,b,c}$. The terminal voltages of the stiff grid are $v_{a,b,c}$.

The control strategy for the PV generator is the typical P&O-based power control. First, the outermost loop is the power loop, which controls the output power of the PV generator and generates reference voltage v_{pv}^{ref} for the middle loop. Due to the intermittency and nonlinearity of the PV

2168-6777 (c) 2019 IEEE. Personal use is permitted, but republication/redistribution requires IEEE permission. See http://www.ieee.org/publications_standards/publications/rights/index.html for more information.

This article has been accepted for publication in a future issue of this journal, but has not been fully edited. Content may change prior to final publication. Citation information: DOI 10.1109/JESTPE.2019.2939379, IEEE Journal of Emerging and Selected Topics in Power Electronics

generator, the P&O-based power control is widely applied. The new grid code regulations require that the PV generators must inject a constant power into the grid to provide reserve service and avoid adverse effects of PV generators with high penetration such as overloading the grid [36]-[37]. That is, if P^{ref} is greater than the maximum power of the PV generator, the PV generator outputs the maximum power. If the P^{ref} is less than the maximum power of the PV generator, the PV generator should output the power P^{ref}. Hence, the studied P&O-based power control has the function of constant power generation. The detailed flow chart is shown in Fig. 2(b), where the perturbation size is ε, and the power control cycle is T_p.

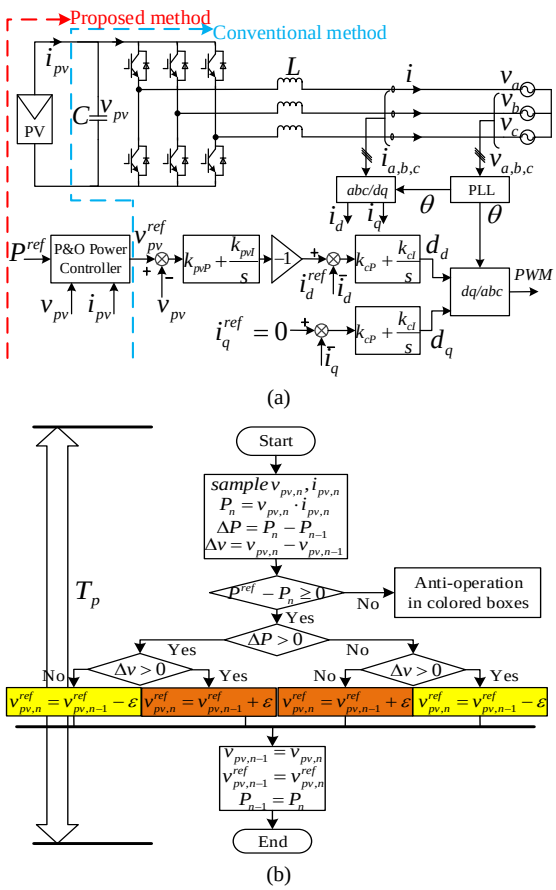

Fig. 2. Topology and control of the studied grid-connected PV generator. (a) Topology and control structure. (b) Flow chart of the P&O-based power control.

Then, the middle loop is the proportional-integral (PI)-based voltage loop, which makes the output voltage of the PV panel v_{pv} track the reference voltage v_{pv}^{ref} accurately and generates reference current i_d^{ref} for the inner loop. Finally, the innermost loop is the PI-based current loop, which regulates the output currents based on the dq synchronous reference frame. The d axis of the synchronous reference frame is orientated to the stiff grid voltage vector. To realize the unity power factor, the reference current i_q^{ref} is set as zero with consideration of the direction of the synchronous reference frame.

Through the above narration, several characteristics of the studied PV generator can be summarized as follows:

(1) The influence of PLL can be avoided because the grid is stiff, and the dynamics of PLL are not influenced by the output of the PV generator. Then, there is no interaction between the PLL and the voltage or current control loop.

(2) The high-order filters are out of consideration since the L-type filter is employed.

(3) The nonlinear discontinuous P&O-based power control and the PV characteristics would be considered carefully, which are hardly researched by the existing literature and are the main points of this paper. The research scope of the proposed method and the conventional method are identified in Fig. 2(a).

According to Fig. 2(a) and the modeling method in [38], the model of the grid-connected PV generator can be derived as

$$\begin{cases} L\dfrac{di_d}{dt} = \omega L i_q + d_d v_{pv} - V \\ L\dfrac{di_q}{dt} = -\omega L i_d + d_q v_{pv} \\ C\dfrac{dv_{pv}}{dt} = i_{pv} - 1.5(d_d i_d + d_q i_q) \end{cases}, \tag{1}$$

where ω is the rated angular frequency and V is the magnitude of the grid voltages $v_{a,b,c}$.

Since (1) is a nonlinear continuous system, the small-signal model can be established at the equilibrium point $(I_d^*, I_q^*, V_{pv}^*, I_{pv}^*\ D_d^*, D_q^*)$,

$$\begin{cases} L\dfrac{d\Delta i_d}{dt} = \omega L \Delta i_q + \Delta d_d V_{pv}^* + D_d^* \Delta v_{pv} \\ L\dfrac{d\Delta i_q}{dt} = -\omega L \Delta i_d + \Delta d_q V_{pv}^* + D_q^* \Delta v_{pv} \\ C\dfrac{d\Delta v_{pv}}{dt} = \Delta i_{pv} - 1.5(\Delta d_d I_d^* + D_d^* \Delta i_d + D_q^* \Delta i_q + \Delta d_q I_q^*) \end{cases}, \tag{2}$$

where $i_d = I_d^* + \Delta i_d$, $i_q = I_q^* + \Delta i_q$, $v_{pv} = V_{pv}^* + \Delta v_{pv}$, $i_{pv} = I_{pv}^* + \Delta i_{pv}$, $d_d = D_d^* + \Delta d_d$ and $d_q = D_q^* + \Delta d_q$.

Considering the model of the PV panel [39], the following equation can be obtained:

$$i_{pv} = N_P(I_{sc} + K_I \Delta T)\left[\frac{G}{G_N} - \frac{\exp(v_{pv}/N_S V_t a) - 1}{\exp((V_{oc} + K_V \Delta T)/V_t a) - 1}\right], \tag{3}$$

where N_P and N_S are the numbers of series and parallel modules. I_{sc} and V_{oc} are the open-circuit voltage and short-circuit current of a PV model. V_t is the thermal voltage, and a is the ideal constant of the equivalent diode. G and G_N are the actual irradiance and the nominal irradiance, respectively. $\Delta T = T - T_N$, where T and T_N are the actual temperature and the nominal temperature, respectively. K_I and K_V are the current and voltage coefficients, respectively. Then, the following expression can be derived.

$$\begin{cases} \Delta P = V_{pv}^* \Delta i_{pv} + \Delta v_{pv} I_{pv}^* = K_{pv} \Delta v_{pv} \\ K_{pv} = g_{pv} V_{pv}^* + P^{ref}/V_{pv}^* \\ g_{pv} = \dfrac{-N_P(I_{sc} + K_I \Delta T)}{\exp((V_{oc} + K_V \Delta T)/V_t a) - 1} \cdot \dfrac{\exp(V_{pv}^*/N_S V_t a)}{N_S V_t a} \end{cases}, \tag{4}$$

where ΔP is the quantity of the small disturbance of the output power of the PV panel.

For convenience, V_{pv}^* and P^{ref} are chosen as known variables. Combining (1) and Fig. 2(a), the other equilibrium points can be calculated as shown below.

$$\begin{cases} I_q^* = 0 \\ I_d^* = P^{ref}/1.5V \\ D_q^* = \omega L I_d^*/V_{pv}^* \\ D_d^* = V/V_{pv}^* \end{cases}. \tag{5}$$

Until now, the open-loop model of the thee-phase PV

2168-6777 (c) 2019 IEEE. Personal use is permitted, but republication/redistribution requires IEEE permission. See http://www.ieee.org/publications_standards/publications/rights/index.html for more information.

This article has been accepted for publication in a future issue of this journal, but has not been fully edited. Content may change prior to final publication. Citation information: DOI 10.1109/JESTPE.2019.2939379, IEEE Journal of Emerging and Selected Topics in Power Electronics

generator has been obtained. Next, the closed-loop model will be derived. Hence, related controllers need to be taken into consideration. With regard to the controller, both the voltage loop and the current loop are linear and are relatively simple. However, the outmost P&O-based power loop is nonlinear and discontinuous and should be modeled properly. From Fig. 2(b), the output of the P&O-based power controller in the continuous domain can be derived as shown below.

$$v_{pv}^{ref} = \frac{\varepsilon}{T_P}\int \mathrm{sgn}(P^{ref} - P_n)\mathrm{sgn}(\Delta P)\mathrm{sgn}(\Delta v)dt, \quad (6)$$

where $\mathrm{sgn}(x)$ is the sign function. If $x \geq 0$, $\mathrm{sgn}(x) = 1$. If $x < 0$, $\mathrm{sgn}(x) = -1$. Through the power-voltage curve of the PV panel shown in Fig. 3, the following equations can be obtained if sampling errors are ignored,

$$\begin{cases} \mathrm{sgn}(\Delta P)\mathrm{sgn}(\Delta v) = 1, & left\ side \\ \mathrm{sgn}(\Delta P)\mathrm{sgn}(\Delta v) = -1, & right\ side \end{cases}. \quad (7)$$

Therefore, based on (7), (6) can be simplified as

$$\begin{cases} v_{pv}^{ref} = \frac{\varepsilon}{T_P}\int \mathrm{sgn}(P^{ref} - P_n)dt, & left\ side \\ v_{pv}^{ref} = \frac{-\varepsilon}{T_P}\int \mathrm{sgn}(P^{ref} - P_n)dt, & right\ side \end{cases}. \quad (8)$$

Equation (8) is nonlinear and discontinuous. Hence, the small-signal modeling cannot be applied anymore. As a result, the conventional stability analysis methods based on the small-signal model usually do not consider the influence of the outermost P&O-based power control loop.

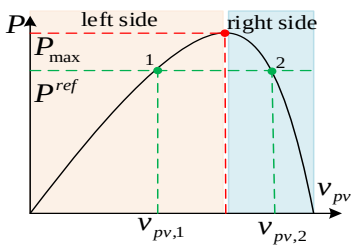

Fig. 3. Power-voltage curve of the PV panel.

Combining (2), (4), (8) and Fig. 2(a), the complete model of the grid-connected PV generator is presented in Fig. 4, when the operation point is located on the left side. The model when the operation point is located on the right side can be derived in the similar way. Fig. 4 shows that the whole system is composed of two parts, namely, the discontinuous sign function based nonlinear part and the small signal based linear part. This structure can be analyzed effectively in the frequency domain by the DF method, which will be introduced in detail in the next section.

For the following comparison, the commonly used model [14]-[16] for the conventional stability analysis methods is also presented in Fig. 5, where the model is consistent with the research scope of the conventional method in Fig. 2(a). Compared to Fig. 4, the model in Fig. 5 has two differences. First, the power loop is removed. Second, the model of the PV panel is simplified into a constant power (CP) model. Based on this purely linear model, some mature analysis methods for the linear system such as the Bode diagram based frequency-domain analysis method can be used to assess the system stability.

III. Describing Method Based Stability Analysis

A. Introduction of the DF Method

In this part, the fundamental principles of the DF method are briefly introduced. Being different from the small-signal analysis which approximates the nonlinear elements in the time domain, the DF method is a kind of frequency-domain approximation. Hence, the DF method can deal with some nonlinear discontinuous elements that cannot be processed by the small-signal modeling in the time domain.

The fundamental principle of the DF method is to obtain the first harmonic component of the output when the nonlinear element is excited with a sinusoidal signal input. As shown in Fig. 6, which is the abstraction of the model in Fig. 4, if the transfer function *G(s)* of the linear part is low-pass, the high-order harmonics produced by the nonlinear element are filtered out. Hence, we can pay the most attention to the first harmonic component of the output of the nonlinear element and research the function of the nonlinear element on the first harmonic component.

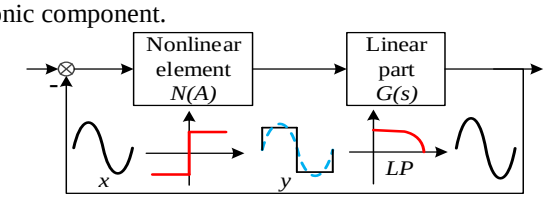

Fig. 6. Response analysis of the system containing the nonlinear discontinuous element.

If the input is $x = A\sin(\omega t)$ and the output is y, we can conclude that y is also a periodic signal. According to the Fourier series, the output y can be decomposed as

$$y = A_0 + \sum_{k=1}^{\infty} A_k \sin(k\omega t + \varphi_k). \quad (9)$$

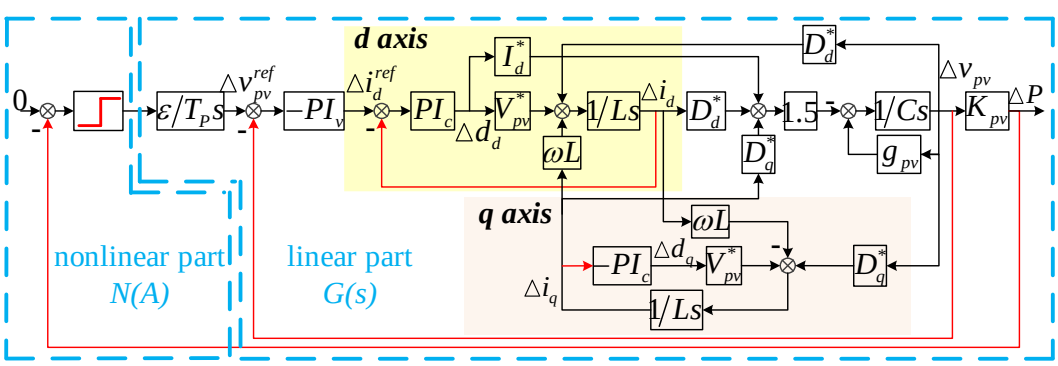

Fig. 4. Complete model of the grid-connected PV generator.

2168-6777 (c) 2019 IEEE. Personal use is permitted, but republication/redistribution requires IEEE permission. See http://www.ieee.org/publications_standards/publications/rights/index.html for more information.

This article has been accepted for publication in a future issue of this journal, but has not been fully edited. Content may change prior to final publication. Citation information: DOI 10.1109/JESTPE.2019.2939379, IEEE Journal of Emerging and Selected Topics in Power Electronics

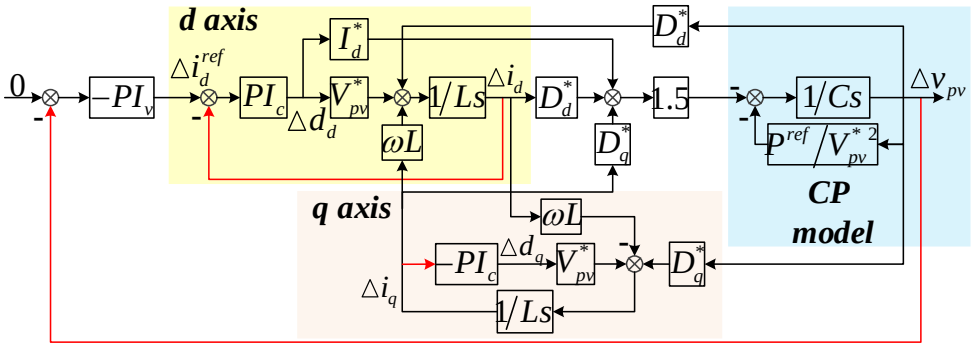

Fig. 5. Conventional stability analysis model of the grid-connected PV generator.

Furthermore, if the nonlinear element is odd-symmetric, the dc component $A_0 = 0$. Then, the function of the nonlinear element on the first harmonic component can be expressed as

$$N(A) = \frac{A_1 e^{j\varphi_1}}{A}, \tag{10}$$

where $N(A)$ is called the describing function of the nonlinear element and can be viewed as a variable gain amplifier in the system.

Based on the describing function $N(A)$ of the nonlinear element, the nonlinear system in Fig. 6 can be approximately transformed into a linear system, in which the forward path is the series connection of $N(A)$ and *G(s)*. The modified Nyquist criterion can be used to assess the system stability according to the relative position of $-1/N(A)$ and *G(s)*, where $-1/N(A)$ is usually a curve in the *s* plane. The modified Nyquist criterion can be expressed as:

(1) If $-1/N(A)$ is not surround by *G(s)*, the system is stable as shown in Fig. 7(a).

(2) If $-1/N(A)$ is surround by *G(s)*, the system is unstable as shown in Fig. 7(b).

(3) If $-1/N(A)$ intersects with *G(s)*, the system is critically stable as shown in Fig. 7(c). Furthermore, the oscillation frequency and magnitude can be calculated through *G(s)* and $-1/N(A)$ at the intersection point, respectively.

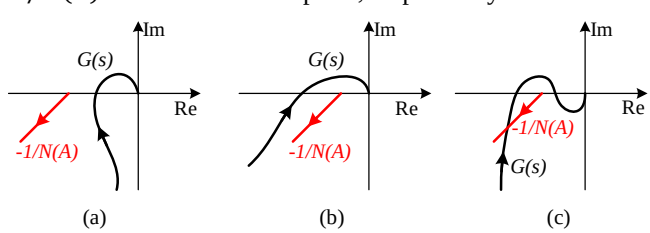

Fig. 7. The DF method-based stability criterion. (a) Stable. (b) Unstable. (c) Critically stable.

For the purely linear system, the criterion of critical stability is very strict because the Nyquist curve of the system must cross the unique point (-1, *j*0) in the whole *s* plane. However, if the nonlinear element is considered based on the DF method, the criterion of critical stability is largely relaxed. Equivalently, the unique point (-1, *j*0) becomes a curve, which enhances the probability of $-1/N(A)$ intersecting with *G(s)*. Hence, the DF method-based stability analysis is more suitable for analyzing critical stability and revealing oscillatory reasons.

In addition, the stability criterion of the DF method does not depend on the stable margin. Hence, DF method can be applied to both the non-minimum and minimum phase systems.

B. Detailed Stability Analysis of the Grid-connected PV Generator

In this part, the detailed stability analysis of the grid-connected PV generator is conducted based on the DF method, and the related influence factors are studied quantitatively. First, the model of the PV generators in Fig. 4 meets the two assumptions of the DF method. That is,

(1) The linear part is low-pass. The output of the PV generator is filtered by the corresponding low-pass filters. Hence, the linear part of the PV generator is low-pass, which can also be verified by the elements of the linear part in Fig. 4.

(2) The nonlinear part is odd-symmetric. Fig. 4 shows that the nonlinear part of the PV generator is a sign function, which is odd-symmetric. Hence, the PV generator meets this requirement as well.

For the linear part in Fig. 4, the detailed expression of *G(s)* is shown in (A.5) of the Appendix. For the sign function in Fig. 4, if the input is $x = A\sin(\omega t)$, then the output of the sign function can be expressed as

$$\begin{cases} y = 1, & 0 \le \omega t \le \pi \\ y = -1, & \pi < \omega t < 2\pi \end{cases}. \tag{11}$$

After Fourier series decomposition of (11) and according to (10), the describing function of the sign function can be obtained as

$$N(A) = \frac{4}{\pi A}. \tag{12}$$

Then, when the system is critically stable, the oscillation magnitude A_o and oscillation frequency ω_o can be calculated by solving the following equations.

$$\begin{cases} G_{Im}(\omega_o) = 0 \\ 4/\pi A_o = -1/G_{Re}(\omega_o) \end{cases}, \tag{13}$$

where $G(j\omega) = G_{Re}(\omega) + jG_{Im}(\omega)$.

The PV module used in this paper is KC200GT, whose detailed parameters are introduced in [38]. The whole PV panel consists of 20 parallel and 60 series KC200GT PV modules. Then, the maximum power of the PV panel can reach approximately 240 kW, and the corresponding voltage v_{pv} is approximately 1680 V under the nominal irradiance $G_N = 1000\ \mathrm{W/m^2}$ and the nominal temperature $T_N = 298.16$ K. The other rated electrical and control parameters of the grid-connected PV generator are shown in Table Ⅰ, where the operation point is indicated by (V_{pv}^*, P^{ref}), and the other equilibrium points can be derived through (5).

2168-6777 (c) 2019 IEEE. Personal use is permitted, but republication/redistribution requires IEEE permission. See http://www.ieee.org/publications_standards/publications/rights/index.html for more information.

This article has been accepted for publication in a future issue of this journal, but has not been fully edited. Content may change prior to final publication. Citation information: DOI 10.1109/JESTPE.2019.2939379, IEEE Journal of Emerging and Selected Topics in Power Electronics

TABLE Ⅰ
RATED SYSTEM PARAMETERS

Parameters	Rated Value
V, ω	311 V, 100π rad/s
C, L	3 mF, 2 mH
G, T	1000 W/m^2 (G_N), 298.16 K (T_N)
(V_{pv}^*, P^{ref})	(1096 V, 180 kW)
g_{pv}	-0.0004 A/V
K_{pv}	163.6 W/V
Power Loop	$\varepsilon = 0.5$ V, $T_P = 0.2$ ms
Voltage Loop	$k_{pvP} = 0.4$ A/V, $k_{pvI} = 80$ A/Vs
Current Loop	$k_{cP} = 0.01$ V/A, $k_{cI} = 0.5$ V/As

1) Operation points

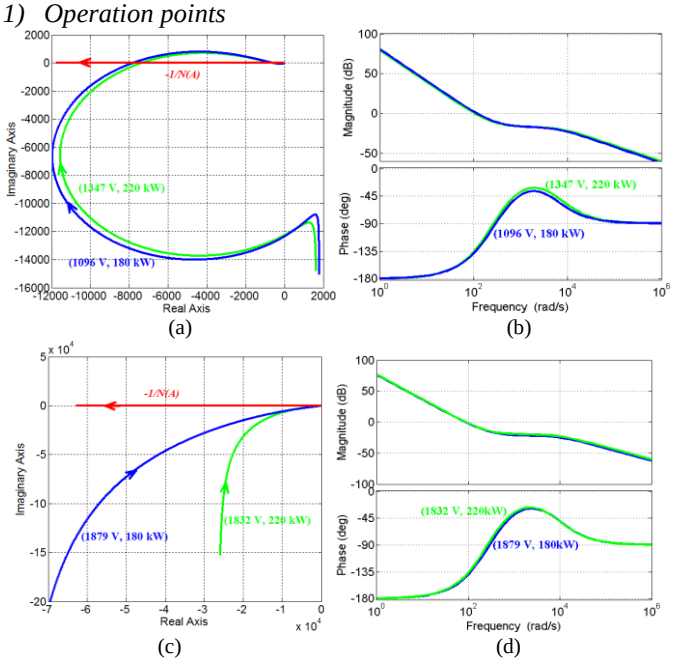

Fig. 8. System stability with changes in the operation points. The proposed analysis method: (a) Nyquist diagrams at the left-side operation points (1096 V, 180 kW), (1347 V, 220 kW) and (c) Nyquist diagrams at the right-side operation points (1879 V, 180 kW), (1832 V, 220 kW). The conventional analysis method: (b) Bode diagrams at the left-side operation points (1096 V, 180 kW), (1347 V, 220 kW) and (d) Bode diagrams at the right-side operation points (1879 V, 180 kW), (1832 V, 220 kW).

The influence of operation points is studied in this small part. Except the operation points and the dependent parameters g_{pv}, K_{pv}, the other parameters remain the same as in Table Ⅰ. Four operation points are chosen, namely, left-side points (1096 V, 180 kW) and (1347 V, 220 kW), right-side points (1879 V, 180 kW) and (1832 V, 220 kW). For these operation points, based on (A.5) of the Appendix, the corresponding linear parts *G(s)* are

$$\begin{cases} G_1(s) = \dfrac{3.2*10^8(s+5445)(s+403)(s+200)(s+50.4)(s+50)}{s(s+5996)(s+5662)(s^2+101.2s+2561)(s^2+32s+9878)} \\ G_2(s) = \dfrac{3.7*10^8(s+6685)(s+329.7)(s+200)(s+50.4)(s+50)}{s(s+7450)(s+6832)(s^2+100.8s+2544)(s^2+31s+8088)} \\ G_3(s) = \dfrac{-2.1*10^9(s+9345)(s+403)(s+200)(s+50.3)(s+50)}{s(s+9921)(s+9526)(s+193)(s+31.7)(s^2+100.3s+2524)} \\ G_4(s) = \dfrac{-1.5*10^9(s+9110)(s+329.7)(s+200)(s+50.3)(s+50)}{s(s+9901)(s+9245)(s+55)(s+47.5)(s^2+151.6s+5961)} \end{cases}. \quad (14)$$

Based on (14), the Nyquist diagrams of the complete model of the grid-connected PV generator are shown in Fig. 8(a) and (c). According to the modified Nyquist criterion, from Fig. 8(a) and $G_1(s)$ and $G_2(s)$ in (14), we can conclude that the system is critically stable when the operation points are located on the left side. Under the same output power, from Fig. 8(c) and $G_3(s)$ and $G_4(s)$ in (14), the system is stable when the operation points are located on the right side. Combining (13) and $G_1(s)$ and $G_2(s)$ in (14), the oscillation magnitude and frequency at (1096 V, 180 kW) and (1347 V, 220 kW) can be calculated, respectively, as

$$\begin{cases} A_{o1} = 10 \text{ kW} \\ \omega_{o1} = 117 \text{ rad/s} \end{cases}, \begin{cases} A_{o2} = 9.6 \text{ kW} \\ \omega_{o2} = 107 \text{ rad/s} \end{cases}. \quad (15)$$

Therefore, we can conclude that the system is more stable when the operation points are located on the

Under the same operation points, Fig. 8(b) and (d) show open-loop Bode diagrams of the system according to the conventional analysis method in Fig. 5, where the corresponding open-loop transfer functions $T(s)$ are

$$\begin{cases} T_1(s) = \dfrac{772(s+5445)(s+403)(s+200)(s+50.4)(s+50)}{s^2(s+53)(s+51)(s^2+10^4s+3*10^7)} \\ T_2(s) = \dfrac{943(s+6685)(s+329.7)(s+200)(s+50.4)(s+50)}{s^2(s^2+102s+2616)(s^2+1.3*10^4s+4.5*10^7)} \\ T_3(s) = \dfrac{772(s+9345)(s+403)(s+200)(s+50.3)(s+50)}{s^2(s^2+101s+2556)(s^2+1.9*10^4s+8.6*10^7)} \\ T_4(s) = \dfrac{943(s+9110)(s+329.7)(s+200)(s+50.3)(s+50)}{s^2(s^2+101s+2558)(s^2+1.8*10^4s+8.3*10^7)} \end{cases}. \quad (16)$$

These two figures show that the system is stable no matter where the operation points are located, and the changes in the operation points have no obvious influence on the system stability, which conflicts with the conclusion of the proposed analysis method. However, according to the experimental results, the conclusion of the proposed analysis method is more accurate.

2) Filters

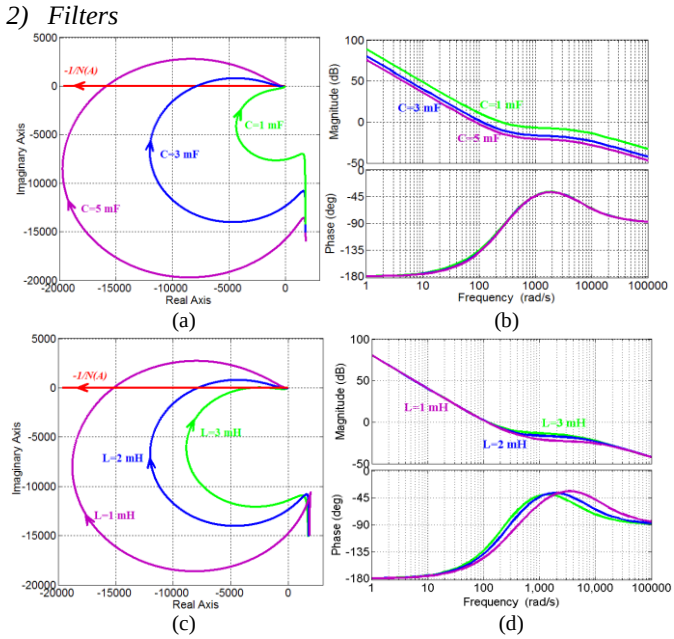

Fig. 9. System stability with changes of filters. The proposed analysis method: (a) Nyquist diagrams when C=1, 3, 5 mF, and (c) Nyquist diagrams when L=1, 2, 3 mH, respectively. The conventional analysis method: (b) Bode diagrams when C=1, 3, 5 mF, and (d) Bode diagrams when L=1, 2, 3 mH, respectively.

2168-6777 (c) 2019 IEEE. Personal use is permitted, but republication/redistribution requires IEEE permission. See http://www.ieee.org/publications_standards/publications/rights/index.html for more information.

This article has been accepted for publication in a future issue of this journal, but has not been fully edited. Content may change prior to final publication. Citation information: DOI 10.1109/JESTPE.2019.2939379, IEEE Journal of Emerging and Selected Topics in Power Electronics

The influence of filters is studied in this small part, including the PV-side capacitor and the grid-side inductor, where the parameters are kept the same as Table Ⅰ except *C* and *L*. Fig. 9(a) and (c) present the Nyquist diagrams of the complete model of the grid-connected PV generator in Fig. 4 with changes of the capacitive filter *C* and the inductive filter *L*, respectively. Based on (A.5) of the Appendix, the corresponding linear parts *G(s)* when *C*=1 mF, 5 mF and *L*= 1, 3 mH are

$$\begin{cases} G_5(s) = \frac{9.5*10^8(s+5445)(s+403)(s+200)(s+50.5)(s+50)}{s(s+7616)(s+5509)(s^2+101.2s+2567)(s^2+78.9s+2.4*10^4)} \\ G_6(s) = \frac{1.9*10^8(s+5445)(s+403)(s+200)(s+50.5)(s+50)}{s(s^2+101.1s+2557)(s^2+20s+6235)(s^2+1.1*10^4s+3.2*10^7)} \\ G_7(s) = \frac{3.2*10^8(s+1.1*10^4)(s+806)(s+200)(s+50.2)(s+50)}{s(s+1.2*10^4)(s+1.1*10^4)(s^2+101s+2549)(s^2+21.7s+1*10^4)} \\ G_8(s) = \frac{3.2*10^8(s+3613)(s+268.7)(s+200)(s+50.7)(s+50)}{s(s+4087)(s+3869)(s^2+101.3s+2569)(s^2+41.27s+9349)} \end{cases}. \quad (17)$$

In Fig. 9(b) and (d), the open-loop Bode diagrams of the system based on the conventional analysis method in Fig. 5 are shown with changes of *C* and *L*, respectively. Similarly, the corresponding open-loop transfer functions *T(s)* when *C*=1 mF, 5 mF and *L*= 1, 3 mH are

$$\begin{cases} T_5(s) = \frac{2315(s+5445)(s+403)(s+200)(s+50.5)(s+50)}{s^2(s+61)(s+49)(s^2+1.1*10^4s+3.1*10^7)} \\ T_6(s) = \frac{463(s+5445)(s+403)(s+200)(s+50.5)(s+50)}{s^2(s^2+102.6s+2635)(s^2+1.1*10^4s+2.99*10^7)} \\ T_7(s) = \frac{772(s+1.1*10^4)(s+806)(s+200)(s+50.2)(s+50)}{s^2(s+54)(s+50.3)(s^2+2.2*10^4s+1.2*10^8)} \\ T_8(s) = \frac{772(s+3613)(s+268.7)(s+200)(s+50.7)(s+50)}{s^2(s^2+103.8s+2698)(s^2+7273s+1.3*10^7)} \end{cases}. \quad (18)$$

From Fig. 9(a) and $G_5(s)$ in (17), when *C*=1 mF, the system is stable. However, with the increase of *C*, the system becomes critically stable. The oscillation magnitude A_{o1} and frequency ω_{o1} when *C*= 3 mF has been calculated in (15). The oscillation magnitude and frequency when *C*= 5 mF can also be calculated according to (13) and $G_6(s)$ in (17).

$$\begin{cases} A_{o3} = 20\ \text{kW} \\ \omega_{o3} = 86\ \text{rad/s} \end{cases}. \quad (19)$$

Compared to A_{o1} and ω_{o1}, we can conclude that with the increase of C, the oscillation magnitude obviously increases, and the oscillation frequency moves toward the low-frequency modes.

Based on the conventional analysis method shown in Fig. 9(b), with the increase of *C*, the magnitude of the open-loop transfer function decreases continuously. Then, the phase margin decreases. According to the figure, the phase margin and the corresponding cutoff frequency when *C*= 3, 5 mF are

$$\begin{cases} P_{m1} = 46.3^\circ \\ \omega_{pm1} = 115\ \text{rad/s} \end{cases}, \begin{cases} P_{m2} = 35.6^\circ \\ \omega_{pm2} = 86\ \text{rad/s} \end{cases}. \quad (20)$$

From (20), the phase margin of the system is reduced with the increase of *C*, but we cannot directly judge that the system is stable or not only through this information. However, through the proposed DF method, the system stability can be reflected directly. Furthermore, comparing ω_{o1} and ω_{pm1}, ω_{o3} and ω_{pm2}, the oscillation frequency obtained from the proposed analysis method coincides with the possible oscillation frequency obtained from the conventional analysis method. However, the conventional analysis method cannot provide information about the oscillation magnitude.

Based on Fig. 9(c) and $G_7(s)$ and $G_8(s)$ in (17), with the increase of *L*, the system is more and more stable. The oscillation magnitude and frequency when *L*= 1, 3 mH can be calculated according to (13) and $G_7(s)$ and $G_8(s)$ in (17).

$$\begin{cases} A_{o4} = 17\ \text{kW} \\ \omega_{o4} = 111\ \text{rad/s} \end{cases}, \begin{cases} A_{o5} = 5.1\ \text{kW} \\ \omega_{o5} = 139\ \text{rad/s} \end{cases}. \quad (21)$$

Combining the oscillation magnitude A_{o1} and frequency ω_{o1} when *L*= 2 mH in (15), we can conclude that the oscillation magnitude is reduced, and the oscillation frequency is raised with the increase of *L*.

Similarly, the open-loop Bode diagrams of the system according to the conventional analysis method are shown in Fig. 9(d) with changes of *L*. The figure shows that with the increase of *L*, the phase of the open-loop transfer function increases continuously. Hence, the phase margin is enhanced, and the system stability is improved. The figure shows that the cutoff frequency when *L*= 1, 2, 3 mH is almost unchanged, and it is approximately 114 rad/s, which is the possible oscillation frequency according to the conventional analysis method. This conclusion conflicts with the conclusion from the proposed analysis method as shown in (21), but according to the experimental results, the conclusion of the proposed analysis method is more accurate.

3) Control parameters

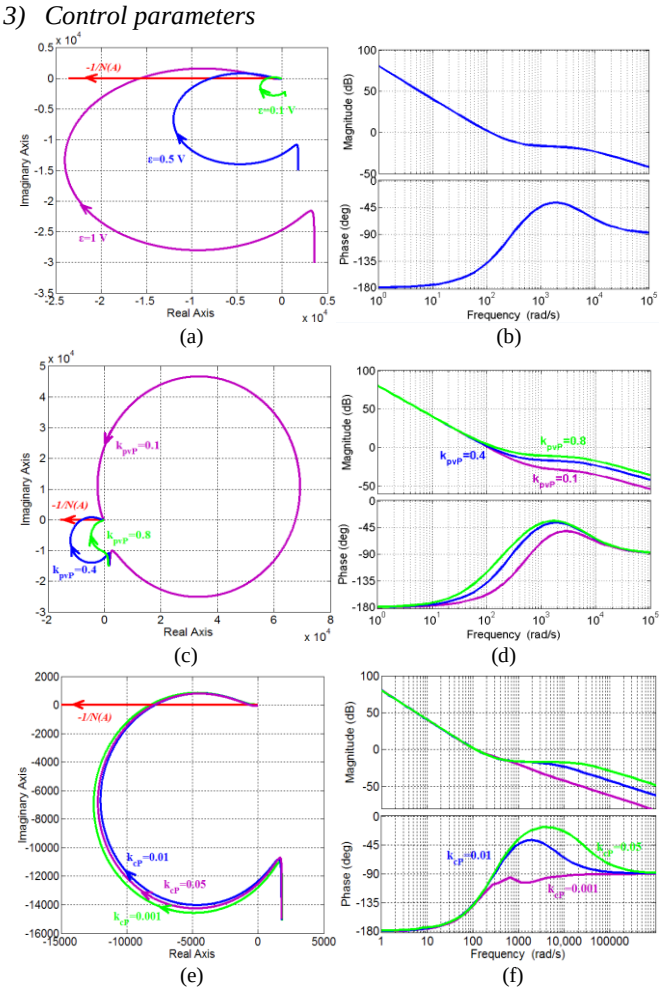

Fig. 10. System stability with changes of control parameters. The proposed analysis method: (a) Nyquist diagrams when ε=0.1, 0.5, 1 V, (c) Nyquist diagrams when $k_{pvP} = 0.1, 0.4, 0.8$ A/V; and (e) Nyquist diagrams when $k_{cP} = 0.001, 0.01, 0.05$A/V; The conventional analysis method: (b) Bode

2168-6777 (c) 2019 IEEE. Personal use is permitted, but republication/redistribution requires IEEE permission. See http://www.ieee.org/publications_standards/publications/rights/index.html for more information.

This article has been accepted for publication in a future issue of this journal, but has not been fully edited. Content may change prior to final publication. Citation information: DOI 10.1109/JESTPE.2019.2939379, IEEE Journal of Emerging and Selected Topics in Power Electronics

diagrams when ε=0.1, 0.5, 1 V; (d) Bode diagrams when k_{pvP} = 0.1, 0.4, 0.8A/V and (f) Bode diagrams when $k_{cP} = 0.001, 0.01, 0.05\text{A/V}$.

In this small part, the influence of the control parameters is studied, where the other parameters are kept the same as Table Ⅰ except the chosen parameters. Fig. 10(a), (c) and (e) shows the Nyquist diagrams of the complete model of the grid-connected PV generator as presented in Fig. 4 with changes of control parameters ε, k_{pvP} and k_{cP}, while Fig. 10(b), (d) and (f) shows the Bode diagrams of the system based on the conventional analysis method as presented in Fig. 5 with changes of these control parameters. When ε changes, from (A.5) of Appendix, for the linear part *G(s)*, only the coefficient ε/T_p will change, and the other zeros/poles stay the same. When $k_{pvP} = 0.1, 0.8\text{A/V}$ and $k_{cP} = 0.001, 0.05\ \text{V/A}$, based on (A.5) of Appendix, the corresponding linear parts *G(s)* are:

$$\begin{cases} G_9(s) = \frac{7.9*10^7(s+5445)(s+800)(s+403)(s+50.5)(s+50)}{s(s^2+101.1s+2556)(s^2+1.1*10^4s+3.1*10^7)(s^2-6.1s+1.1*10^4)} \\ G_{10}(s) = \frac{6.3*10^8(s+5445)(s+403)(s+100)(s+50.5)(s+50)}{s(s+6832)(s+5527)(s^2+101.3s+2570)(s^2+73.4s+8805)} \\ G_{11}(s) = \frac{3.2*10^7(s+500)(s+403)(s+200)(s^2+550s+2.7*10^5)}{s(s^2+32s+9716)(s^2+374s+1.5*10^4)(s^2+770s+6*10^5)} \\ G_{12}(s) = \frac{1.6*10^9(s+2.7*10^4)(s+403)(s+200)(s+10)^2}{s(s+3.1*10^4)(s+2.7*10^4)(s^2+20s+100)(s^2+31s+9931)} \end{cases}. \quad (22)$$

Similarly, the corresponding open-loop transfer functions *T(s)* for the conventional analysis method are:

$$\begin{cases} T_9(s) = \frac{193(s+5445)(s+800)(s+403)(s+50.5)(s+50)}{s^2(s+53)(s+51)(s^2+1.1*10^4s+3.0*10^7)} \\ T_{10}(s) = \frac{1543(s+5445)(s+403)(s+100)(s+50.5)(s+50)}{s^2(s+53)(s+51)(s^2+1.1*10^4s+3.0*10^7)} \\ T_{11}(s) = \frac{77(s+500)(s+403)(s+200)(s^2+550s+2.7*10^5)}{s^2(s^2+393s+1.4*10^5)(s^2+756s+5.7*10^5)} \\ T_{12}(s) = \frac{3858(s+2.7*10^4)(s+403)(s+200)(s+10)^2}{s^2(s+11)(s+9.9)(s^2+5.5*10^4s+7.6*10^8)} \end{cases}. \quad (23)$$

Fig. 10(a) shows the critical stability of the system with changes of perturbation size ε in the power loop. When ε=0.1 V, the oscillation is very small and can be neglected. With the increase of ε, which means that the bandwidth of the outer loop increases, the oscillation is more and more obvious. The concrete oscillation frequency and magnitude when ε= 1 V are:

$$\begin{cases} A_{o6} = 19\ \text{kW} \\ \omega_{o6} = 118\ \text{rad/s} \end{cases}. \quad (24)$$

Combing the oscillation magnitude A_{o1} and the frequency ω_{o1} when ε= 0.5 V in (15), we can conclude that with the increase of ε, the oscillation magnitude obviously increases, but the oscillation frequency remains almost unchanged.

Since the conventional analysis method does not include the dynamics of the nonlinear discontinuous power control, the influence of perturbation size ε cannot be studied. As shown in Fig. 10(b), the open-loop Bode diagrams are unchanged. However, as analyzed above, the nonlinear discontinuous power loop has a significant influence on the system stability. Therefore, it is an obvious drawback of the conventional analysis method.

Fig. 10(c) shows the influence of k_{pvP} in the voltage loop. When $k_{pvP} = 0.1\ \text{A/V}$, although the Nyquist curve of the system does not surround *-1/N(A)*, *G(s)* has the right-half-plane poles, as $G_9(s)$ in (22) shows. Therefore, the system is unstable. With the increase in k_{pvP}, which means that the bandwidth of the inner loop increases, the system becomes critically stable. With the further increase, the system is stable when $k_{pvP} = 0.8\ \text{A/V}$. Therefore, we can conclude that with the increase of k_{pvP}, the oscillation can be suppressed.

Fig. 10(d) shows the results of the conventional analysis method when k_{pvP} changes. The figure shows that with the increase of k_{pvP}, the phase margin of the system is enhanced continuously. However, just by the Bode diagrams, the variation tendency of the system stability is hard to reflect.

Fig. 10(e) shows the influence of k_{cP} in the current loop, where $k_{cP} = 0.001, 0.01, 0.05\ \text{V/A}$. The changes of k_{cP} have no obvious influence on the system stability. In Fig. 10(f), the results of the conventional analysis method are presented when k_{cP} changes. The figure shows that the changes of k_{cP} mainly influence the high-frequency section but have less influence on the low-frequency section. Hence, k_{cP} has no obvious influence on the low-frequency power oscillation, which also coincides with the conclusion of the proposed analysis method.

IV. Hardware-in-loop Tests

To verify the theoretical analyses, the corresponding HIL tests were conducted. As shown in Fig. 11, the HIL platform consists of the RTLAB and TMS320F28335 DSPs. The topology and the control method of the grid-connected three-phase PV generator are shown in Fig. 2, and the related parameters are the same as Table Ⅰ except for the variable parameters studied in different cases. The main loop is realized in RTLAB, which can output the related electrical signals and accept the control signals, namely, the PWM. The control algorithm is written in the TMS320F28335 DSPs, which can sample the electrical signals and execute the control algorithm. Then, the PWM is generated to control the PV generator.

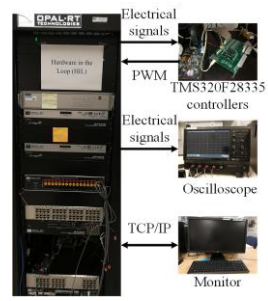

Fig. 11. HIL platform setup.

Fig. 12 shows the system dynamics with changes of the operation points. Fig. 12(a) shows the output power and PV voltage under the left-side operation points (1096 V, 180 kW) and (1347 V, 220 kW), in which $\Delta P = P - 180\text{kW}$ and $\Delta v_{pv} = v_{pv} - 1100\text{V}$. The figure clearly shows that the system is critically stable, both the output power and PV voltage obviously oscillate, which coincides with the theoretical analysis in Fig. 8(a). When the operation point is (1096 V, 180 kW), the oscillation magnitude and frequency are approximately 10 kW and 121 rad/s. For the operation point (1347 V, 220 kW), the oscillation magnitude almost remains the same, but the oscillation frequency becomes 110 rad/s. These two experimental results can meet the theoretical calculation in (15) well, which proves that the proposed

2168-6777 (c) 2019 IEEE. Personal use is permitted, but republication/redistribution requires IEEE permission. See http://www.ieee.org/publications_standards/publications/rights/index.html for more information.

This article has been accepted for publication in a future issue of this journal, but has not been fully edited. Content may change prior to final publication. Citation information: DOI 10.1109/JESTPE.2019.2939379, IEEE Journal of Emerging and Selected Topics in Power Electronics

analysis method can provide accurate oscillation information.

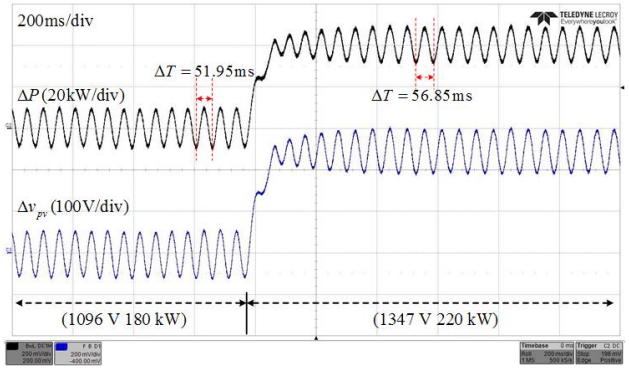

(a)

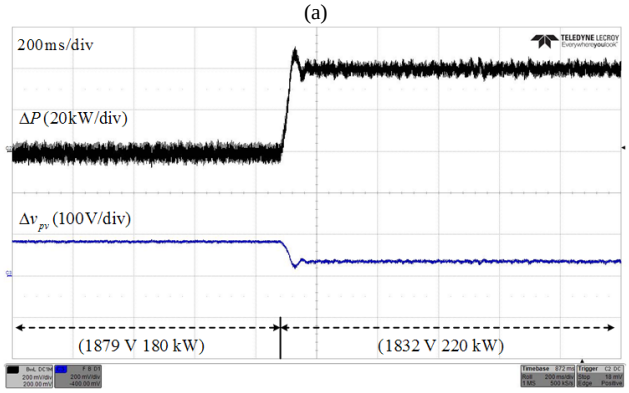

(b)

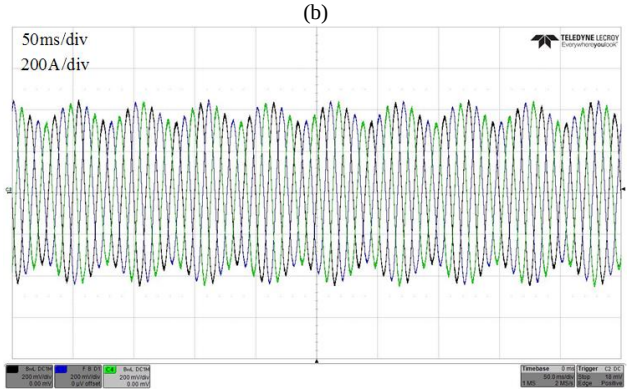

(c)

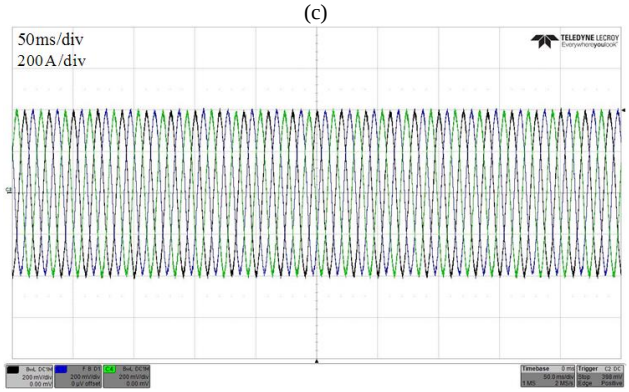

(d)

Fig. 12. System dynamics with changes of operation points. (a) Output power and PV voltage under the left-side operation points (1096 V, 180 kW) and (1347 V, 220 kW). (b) Output power and PV voltage under the right-side operation points (1879 V 180 kW) and (1832 V, 220 kW). (c) Output three-phase currents under operation point (1096 V, 180 kW). (d) Output three-phase currents under operation point (1879 V, 180 kW).

Fig. 12(b) shows the output power and PV voltage under the right-side operation points (1879 V, 180 kW) and (1832 V, 220 kW), in which $\Delta P = P - 180\text{kW}$ and $\Delta v_{pv} = v_{pv} - 1800\text{V}$. Under the same output power, the right-side operation points can make the system stable compared to the left-side operation points. This conclusion about the influence of operation points cannot be obtained from the conventional analysis method as shown in Fig. 8(b) and (d), but the proposed analysis method can analyze the influence of operation points well as shown in Fig. 8(a) and (c). That is, the proposed analysis method can enhance the accuracy of the stability assessment.

Fig. 12(c) and (d) show the output three-phase currents of the grid-connected PV generator under the operation points (1096 V, 180 kW) and (1879 V, 180 kW), respectively. The system is critically stable under the operation point (1096 V, 180 kW), thus the output three-phase currents obviously fluctuate with low frequency at approximately 121 rad/s. However, the system is stable under the operation point (1879 V, 180 kW). Hence, the output currents are smooth without fluctuation. In conclusion, the system stability can be enhanced when the operation points move toward the right side.

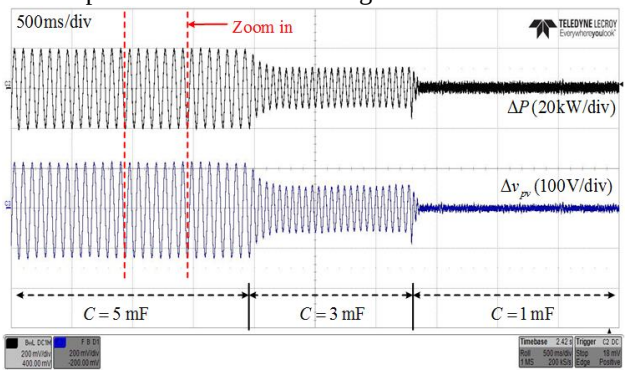

(a)

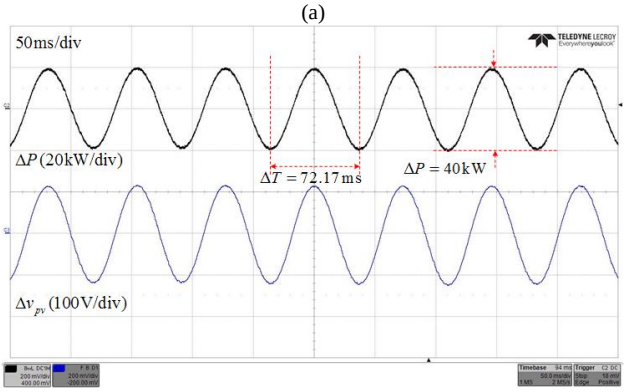

(b)

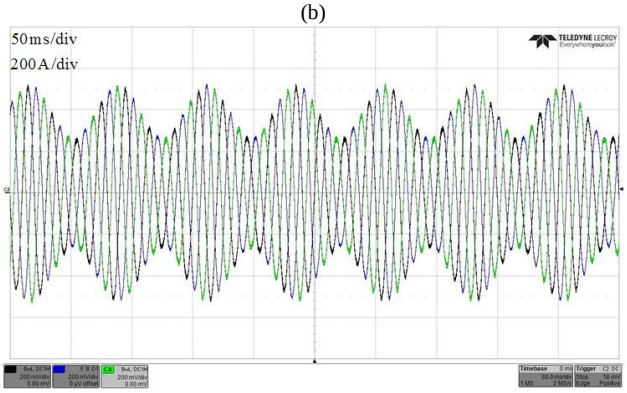

(c)

2168-6777 (c) 2019 IEEE. Personal use is permitted, but republication/redistribution requires IEEE permission. See http://www.ieee.org/publications_standards/publications/rights/index.html for more information.

This article has been accepted for publication in a future issue of this journal, but has not been fully edited. Content may change prior to final publication. Citation information: DOI 10.1109/JESTPE.2019.2939379, IEEE Journal of Emerging and Selected Topics in Power Electronics

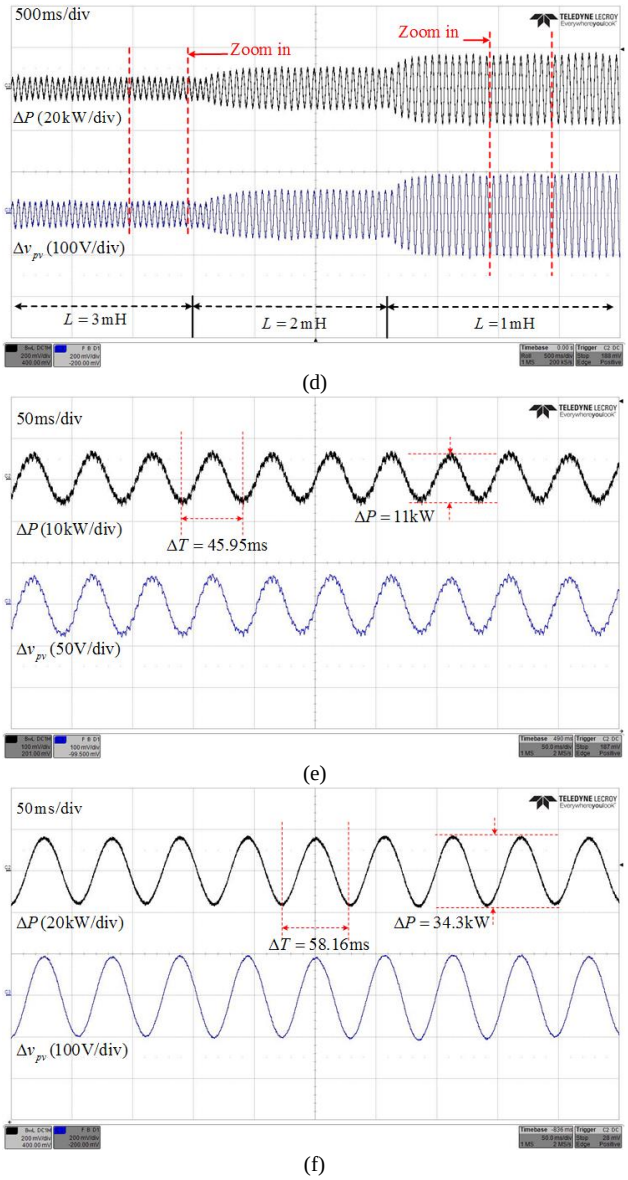

Fig. 13. System dynamics with changes of filters. (a) Output power and PV voltage when C=5, 3, 1 mF. (b) Enlarged version when C=5 mF. (c) Output three-phase currents when C=5 mF. (d) Output power and PV voltage when L=3, 2, 1 mH. (e) Enlarged version when L=3 mH. (f) Enlarged version when L=1 mH.

Fig. 13 shows the system dynamics with changes of filters C and L. Fig. 13(a) shows the output power and PV voltage when C=5, 3, 1 mF, in which $\Delta P = P - 180\text{kW}$ and $\Delta v_{pv} = v_{pv} - 1100\text{V}$. With the decrease of C, the oscillation is reduced. When C=1 mF, the system becomes stable, and the oscillation is completely suppressed. The tendency to stability with changes of C is in accord with the theoretical analysis revealed in Fig. 9(a), and the stability can be directly reflected without stable margin or similar posteriori information.

Fig. 13(b) presents the enlarged version when C=5 mF. As shown in the figure, the measured magnitude of the oscillation and frequency are 20 kW and 87 rad/s, both of which coincide with the theoretical calculation of the proposed DF method based analysis method presented in (19). Especially, the magnitude information is difficult to obtain by the conventional analysis method. That is, the proposed DF method based analysis method can provide more stability information compared to the conventional analysis method. In Fig. 13(c), the output three-phase currents are shown when C=5 mF. Compared to the output currents in Fig. 12(c), namely, the output currents when C=3 mF, the oscillation magnitude is obviously increased, and the oscillation frequency becomes lower. Fig. 13(b) presents the enlarged version when C=5 mF. As shown in the figure, the measured magnitude of the oscillation and frequency are 20 kW and 87 rad/s, both of which coincide with the theoretical calculation of the proposed DF method based analysis method presented in (19). Especially, the magnitude information is difficult to obtain by the conventional analysis method. That is, the proposed DF method based analysis method can provide more stability information compared to the conventional analysis method. In Fig. 13(c), the output three-phase currents are shown when C=5 mF. Compared to the output currents in Fig. 12(c), namely, the output currents when C=3 mF, the oscillation magnitude is obviously increased, and the oscillation frequency becomes lower.

Fig. 13(d) shows the output power and PV voltage when L=3, 2, 1 mH, respectively, in which $\Delta P = P - 180\text{kW}$ and $\Delta v_{pv} = v_{pv} - 1100\text{V}$. The figure shows that with the decrease of L, the oscillation is more and more obvious, which meets the theoretical analysis revealed in Fig. 9(c) well. Through the enlarged version when L=3 mH and L=1 mH in Fig. 13(e) and Fig. 13(f), respectively, the magnitude of the oscillation and frequency are 5.5 kW and 137 rad/s when L=3 mH, 17.15 kW and 108 rad/s when L=1 mH. These results are in accord with the theoretical calculation in (21). However, through the conventional analysis method presented in Fig. 9(d), the relationship of stability and L cannot be explored well. This comparison further proves that the proposed analysis method can enhance the accuracy of the stability assessment.

In conclusion, the system stability is significantly related to the filters, both the oscillation magnitude and the frequency will be obviously varied when the filters are changed. Furthermore, the system stability can be enhanced through decreasing C and increasing L.

Fig. 14 shows the system dynamics with changes of control parameters. Fig. 14 (a) shows the output power and PV voltage when ε=0.1, 0.5, 1 V respectively, in which $\Delta P = P - 180\text{kW}$ and $\Delta v_{pv} = v_{pv} - 1100\text{V}$. Through these results, it can be seen that when ε=0.1 V, the oscillation is very small. With the increase of ε, that is, the equivalent bandwidth of the outer loop (power loop) is increased, the oscillation is increasingly obvious, which is in accord with the theoretical analysis revealed in Fig. 10(a). Since the power control is based on the P&O method that is nonlinear and discontinuous, the conventional small signal-based analysis method cannot analyze the influence of ε. Fig. 14(b) shows the enlarged version when ε=1 V, through which the oscillation magnitude and frequency are 19.5 kW and 119 rad/s, respectively. The obtained result meets the theoretical calculation in (24). Through these contrasts between the experimental results and the theoretical calculation, we can conclude that the proposed

2168-6777 (c) 2019 IEEE. Personal use is permitted, but republication/redistribution requires IEEE permission. See http://www.ieee.org/publications_standards/publications/rights/index.html for more information.

This article has been accepted for publication in a future issue of this journal, but has not been fully edited. Content may change prior to final publication. Citation information: DOI 10.1109/JESTPE.2019.2939379, IEEE Journal of Emerging and Selected Topics in Power Electronics

analysis method can predict the system stability accurately and provide enough stability information without the further simulation to provide auxiliary analysis. Hence, it is more convenient.

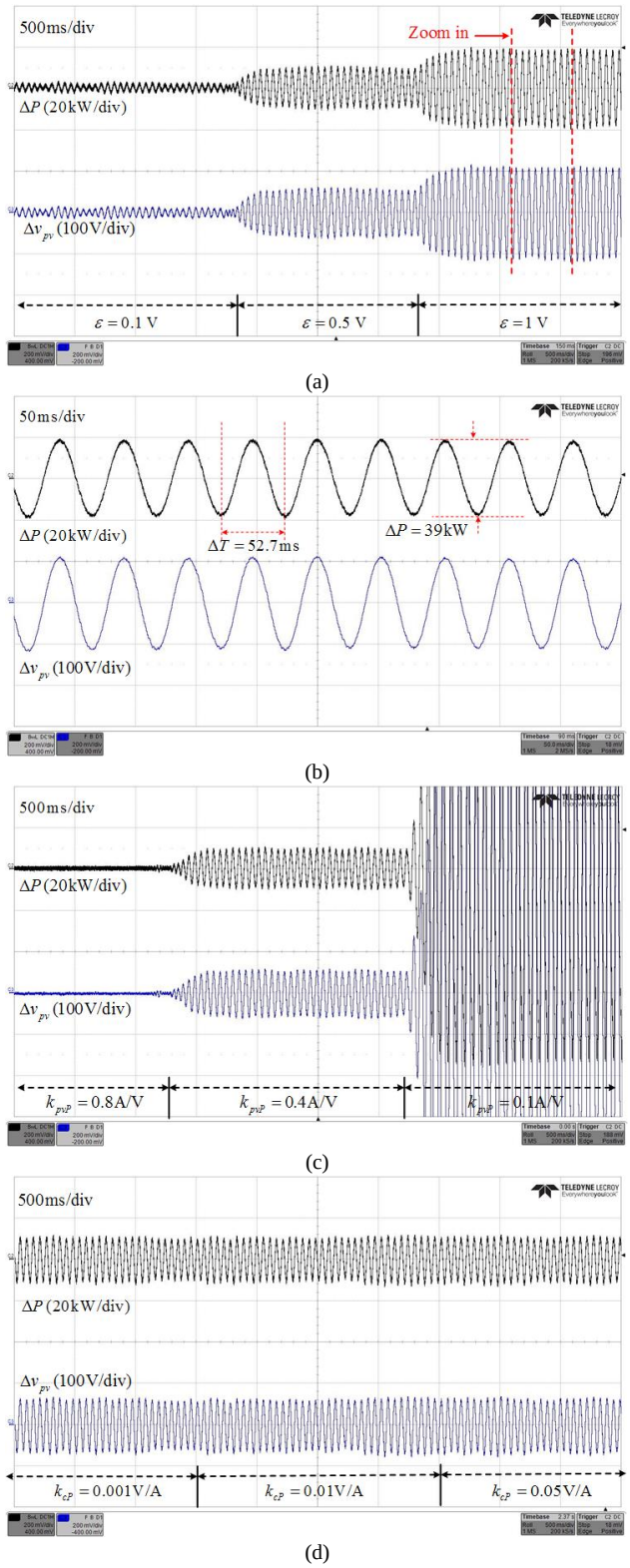

Fig. 14. System dynamics with changes of control parameters. (a) Output power and PV voltage when ε=0.1, 0.5, 1 V. (b) Enlarged version when ε=1 V. (c) Output power and PV voltage when $k_{pvP} = 0.8, 0.4, 0.1$ A/V. (d) Output power and PV voltage when $k_{cP} = 0.001, 0.01, 0.05$ V/A.

Fig. 14(c) shows the output power and PV voltage when $k_{pvP} = 0.8, 0.4, 0.1$ A/V, respectively, in which $\Delta P = P - 180$ kW and $\Delta v_{pv} = v_{pv} - 1100$ V. With the decrease of k_{pvP}, that is, the equivalent bandwidth of the inner loop (voltage loop plus current loop) is decreased, the system is stable, then critically stable and finally unstable. The tendency of stability coincides with the theoretical analysis of the proposed method as shown in Fig. 10(c). However, for the conventional analysis method, the system stability, especially the instability when $k_{pvP} = 0.1$A/V, cannot be well reflected, as shown in Fig. 10(d).

Fig. 14(d) shows the output power and PV voltage when $k_{cP} = 0.001, 0.01, 0.05$ V/A, in which $\Delta P = P - 180$ kW and $\Delta v_{pv} = v_{pv} - 1100$ V. The figure shows that the changes of k_{cP} have no obvious influence on the system stability, which can be explained effectively by both the proposed analysis method and the conventional analysis method.

In conclusion, the control parameters that mainly determine the low-frequency characteristics can influence the system stability. With a smaller bandwidth of the outer loop (like decreasing ε) and bigger bandwidth of the inner loop (like increasing k_{pvP}), the system stability can be enhanced.

V. Conclusion

In this paper, taking the three-phase grid-connected PV generator as the research object, the DF method is adopted to analyze the influence of nonlinear discontinuous elements on system stability when renewable energy sources are integrated into the power system. Then, the drawbacks of the conventional analysis methods can be overcome, and the accuracy of the stability analysis is enhanced. Especially, both the oscillation magnitude and frequency can be calculated out. The typical nonlinear discontinuous element -- P&O-based power control has a substantial influence on the system stability. The power oscillation can occur even when the PV generator is connected to the stiff grid. Through the detailed stability analysis based on the proposed method, the related influence factors such as operation points, filters and control parameters have been studied quantitatively. We conclude that the system stability can be enhanced by: 1) right-side operation points; 2) smaller C and larger L; and 3) smaller bandwidth of the outer loop and bigger bandwidth of the inner loop. Furthermore, through the comparison with the conventional stability analysis method, the superiority of the proposed stability analysis method is clearly illustrated. Finally, the HIL tests were conducted, and the results can verify all the theoretical analyses well.

Appendix

According to (2), the following derivation is presented:

$$\begin{cases} \Delta i_d = H_{dd}(s)\Delta d_d + H_{dq}(s)\Delta d_q \\ \Delta i_q = H_{qd}(s)\Delta d_d + H_{qq}(s)\Delta d_q \\ \Delta v_{pv} = H_{vd}(s)\Delta d_d + H_{vq}(s)\Delta d_q \end{cases}, \tag{A.1}$$

where

$$H_{dd}(s) = \frac{LCV_{pv}^{*}s^2 - L(V_{pv}^{*}g_{pv} + 1.5D_d^{*}I_d^{*})s + 1.5D_q^{*}(D_q^{*}V_{pv}^{*} - I_d^{*}\omega L)}{L^2Cs^3 - L^2g_{pv}s^2 + (1.5LD_d^{*2} + 1.5LD_q^{*2} + \omega^2L^2C)s - \omega^2L^2g_{pv}},$$

2168-6777 (c) 2019 IEEE. Personal use is permitted, but republication/redistribution requires IEEE permission. See http://www.ieee.org/publications_standards/publications/rights/index.html for more information.

This article has been accepted for publication in a future issue of this journal, but has not been fully edited. Content may change prior to final publication. Citation information: DOI 10.1109/JESTPE.2019.2939379, IEEE Journal of Emerging and Selected Topics in Power Electronics

$$H_{dq}(s)=\frac{(\omega LCV_{pv}^{*}-1.5D_d^{*}I_q^{*}L)s-1.5D_q^{*}(D_d^{*}V_{pv}^{*}+I_q^{*}\omega L)-\omega LV_{pv}^{*}g_{pv}}{L^2Cs^3-L^2g_{pv}s^2+(1.5LD_d^{*2}+1.5LD_q^{*2}+\omega^2L^2C)s-\omega^2L^2g_{pv}},$$

$$H_{qd}(s)=\frac{-(\omega LCV_{pv}^{*}+1.5D_q^{*}I_d^{*}L)s-1.5D_d^{*}(D_q^{*}V_{pv}^{*}-I_d^{*}\omega L)+\omega LV_{pv}^{*}g_{pv}}{L^2Cs^3-L^2g_{pv}s^2+(1.5LD_d^{*2}+1.5LD_q^{*2}+\omega^2L^2C)s-\omega^2L^2g_{pv}},$$

$$H_{qq}(s)=\frac{LCV_{pv}^{*}s^2-L(V_{pv}^{*}g_{pv}+1.5D_q^{*}I_q^{*})s+1.5D_d^{*}(D_d^{*}V_{pv}^{*}+I_q^{*}\omega L)}{L^2Cs^3-L^2g_{pv}s^2+(1.5LD_d^{*2}+1.5LD_q^{*2}+\omega^2L^2C)s-\omega^2L^2g_{pv}},$$

$$H_{vd}(s)=\frac{-1.5(I_d^{*}Ls^2+D_d^{*}V_{pv}^{*}s+\omega^2LI_d^{*}-\omega D_q^{*}V_{pv}^{*})}{L^2Cs^3-L^2g_{pv}s^2+(1.5LD_d^{*2}+1.5LD_q^{*2}+\omega^2L^2C)s-\omega^2L^2g_{pv}},$$

$$H_{vq}(s)=\frac{-1.5(I_q^{*}Ls^2+D_q^{*}V_{pv}^{*}s+\omega^2LI_q^{*}+\omega D_d^{*}V_{pv}^{*})}{L^2Cs^3-L^2g_{pv}s^2+(1.5LD_d^{*2}+1.5LD_q^{*2}+\omega^2L^2C)s-\omega^2L^2g_{pv}}.$$

Furthermore, based on Fig. 4, it can be concluded that

$$\begin{cases}\Delta d_d=[(\Delta v_{pv}-\Delta v_{pv}^{ref})PI_{pv}(s)-\Delta i_d]PI_c(s)\\ \Delta d_q=-\Delta i_qPI_c(s)\end{cases},\quad (A.2)$$

Then, combining (A.1) and (A.2), the following equations can be deduced.

$$\begin{cases}\Delta i_q=T_q(s)\Delta d_d=\frac{H_{qd}(s)}{1+H_{qq}(s)PI_c(s)}\Delta d_d\\ \Delta i_d=T_d(s)\Delta d_d=\left[H_{dd}(s)-H_{qd}(s)T_q(s)PI_c(s)\right]\Delta d_d\\ \Delta v_{pv}=T_v(s)\Delta d_d=[H_{vd}(s)-H_{vq}(s)T_q(s)PI_c(s)]\Delta d_d\end{cases}.\quad (A.3)$$

From (A.2) and (A.3), Δd_d can be solved as

$$\Delta d_d=\frac{PI_{pv}(s)PI_c(s)}{T_v(s)PI_{pv}(s)PI_c(s)-T_d(s)PI_c(s)-1}\Delta v_{pv}^{ref},\quad (A.4)$$

Therefore, the transfer function $G(s)$ of the linear part in Fig. 4 can be calculated as:

$$G(s)=\frac{T_v(s)PI_{pv}(s)PI_c(s)}{T_v(s)PI_{pv}(s)PI_c(s)-T_d(s)PI_c(s)-1}\frac{\varepsilon/T_p}{s}.\quad (A.5)$$

In a similar way, the open-loop transfer function in Fig. 5 can also be calculated, and there is no more detailed description here.

REFERENCES

[1] P. -H. Huang, M. S. EI Moursi, W. Xiao, and J. L. Kirtley, “Subsyn-chronous resonance mitigation for series-compensated DFIG-based wind farm by using Two-Degree-of-Freedom control strategy,” *IEEE Trans. Power Syst*., vol. 30, no. 3, pp. 1442-1454, May 2015.

[2] H. K. Liu, X. Xie, J. He, T. Xu, Z. Yu, C. Wang, and C. Zhang, “Sub-synchronous interaction between direct-drive PMSG based wind farms and weak AC networks,” *IEEE Trans. Power Syst*., vol. 32, no. 6, pp. 4708-4720, Nov. 2017.

[3] L. Wang, X. Xie, Q. Jiang, H. Liu, Y. Li, and H. K. Liu, “Investigation of SSR in practical DFIG-based wind farms connected to a se-ries-compensated power system,” *IEEE Trans. Power Syst*., vol. 30, no. 5, pp. 2772-2779, Sept. 2015.

[4] H. K. Liu, X. Xie, C. Zhang, Y. Li, H. Liu, and Y. Hu, “Quantitative SSR analysis of series-compensated DFIG-based wind farms using aggregated *RLC* circuit model,” *IEEE Trans. Power Syst*., vol. 32, no. 1, pp. 474-483, Jan. 2017.

[5] S. Dahal, N. Mithulananthan and T. Saha, "An approach to control a photovoltaic generator to damp low frequency oscillations in an emerging distribution system," *in Proc. IEEE Power Energy Soc. Gen. Meet., Jul. 2011, pp. 1–8.*

[6] S. Liu, P. X. Liu and X. Wang, "Stability Analysis of Grid-Interfacing Inverter Control in Distribution Systems With Multiple Photovoltaic-Based Distributed Generators," *IEEE Trans. Ind. Electron.*, vol. 63, no. 12, pp. 7339-7348, Dec. 2016.

[7] R. Shah, N. Mithulananthan and K. Y. Lee, "Large-Scale PV Plant With a Robust Controller Considering Power Oscillation Damping," *IEEE Trans. Energy Convers.*, vol. 28, no. 1, pp. 106-116, March 2013.

[8] X. Wang, F. Blaabjerg, M. Liserre, Z. Chen, J. He, and Y. Li, “An active damper for stabilizing power-electronics-based AC system,” *IEEE Trans. Power Electro*., vol. 29, no. 7, pp. 3318-3329, July 2014.

[9] N. Rashidirad, M. Hamzeh, K. Sheshyekani and E. Afjei, "High-Frequency Oscillations and Their Leading Causes in DC Microgrids," *IEEE Trans. Energy Convers.*, vol. 32, no. 4, pp. 1479-1491, Dec. 2017.

[10] D. Dong, B. Wen, D. Boroyevich, P. Mattavelli and Y. Xue, "Analysis of Phase-Locked Loop Low-Frequency Stability in Three-Phase Grid-Connected Power Converters Considering Impedance Interactions," *IEEE Trans. Ind. Electron.*, vol. 62, no. 1, pp. 310-321, Jan. 2015.

[11] B. Wen, D. Boroyevich, R. Burgos, P. Mattavelli and Z. Shen, "Analysis of D-Q Small-Signal Impedance of Grid-Tied Inverters," *IEEE Trans. Power Electron.*, vol. 31, no. 1, pp. 675-687, Jan. 2016.

[12] J. Fang, X. Li, H. Li and Y. Tang, "Stability Improvement for Three-Phase Grid-Connected Converters through Impedance Reshaping in Quadrature-Axis," *IEEE Trans. Power Electron.*, vol. 33, no. 10, pp. 8365-8375, Oct. 2018.

[13] D. Shu, X. Xie, H. Rao, X. Gao, Q. Jiang and Y. Huang, "Sub- and Super-Synchronous Interactions between STATCOMs and Weak AC/DC Transmissions with Series Compensations," *IEEE Trans. Power Electron.*, vol. 33, no. 9, pp. 7424-7437, Sept. 2018.

[14] M. Davari and Y. A. R. I. Mohamed, "Robust Vector Control of a Very Weak-Grid-Connected Voltage-Source Converter Considering the Phase-Locked Loop Dynamics," *IEEE Trans. Power Electron.*, vol. 32, no. 2, pp. 977-994, Feb. 2017.

[15] Y. Huang, X. Yuan, J. Hu and P. Zhou, "Modeling of VSC Connected to Weak Grid for Stability Analysis of DC-Link Voltage Control," *IEEE J. Emerg. Sel. Topics Power Electron.*, vol. 3, no. 4, pp. 1193-1204, Dec. 2015.

[16] Y. Huang, X. Yuan, J. Hu, P. Zhou and D. Wang, "DC-Bus Voltage Control Stability Affected by AC-Bus Voltage Control in VSCs Connected to Weak AC Grids," *IEEE J. Emerg. Sel. Topics Power Electron.*, vol. 4, no. 2, pp. 445-458, June 2016.

[17] Y. Tang, P. C. Loh, P. Wang, F. H. Choo and F. Gao, "Exploring Inherent Damping Characteristic of LCL-Filters for Three-Phase Grid-Connected Voltage Source Inverters," *IEEE Trans. Power Electron.*, vol. 27, no. 3, pp. 1433-1443, March 2012.

[18] X. Li, J. Fang, Y. Tang, X. Wu and Y. Geng, "Capacitor-Voltage Feedforward With Full Delay Compensation to Improve Weak Grids Adaptability of LCL-Filtered Grid-Connected Converters for Distributed Generation Systems," *IEEE Trans. Power Electron.*, vol. 33, no. 1, pp. 749-764, Jan. 2018.

[19] A. Aapro, T. Messo, T. Roinila and T. Suntio, "Effect of Active Damping on Output Impedance of Three-Phase Grid-Connected Converter," *IEEE Trans. Power Electron.*, vol. 64, no. 9, pp. 7532-7541, Sept. 2017.

[20] F. D. Freijedo, E. Rodriguez-Diaz, M. S. Golsorkhi, J. C. Vasquez and J. M. Guerrero, "A Root-Locus Design Methodology Derived From the Impedance/Admittance Stability Formulation and Its Application for LCL Grid-Connected Converters in Wind Turbines," *IEEE Trans. Power Electron.*, vol. 32, no. 10, pp. 8218-8228, Oct. 2017.

[21] S. Zhou *et al*., "An Improved Design of Current Controller for LCL-Type Grid-Connected Converter toReduce Negative Effect of PLL in Weak Grid," *IEEE J. Emerg. Sel. Topics Power Electron.*, vol. 6, no. 2, pp. 648-663, June 2018.

[22] Y. Xia, M. Yu, X. Wang and W. Wei, "Describing Function Method Based Power Oscillation Analysis of LCL-Filtered Single-Stage PV Generators Connected to Weak Grid," *IEEE Trans. Power Electron.*, vol. 34, no. 9, pp. 8724-8738, Sept. 2019.

[23] H. Liu, X. Xie and W. Liu, "An Oscillatory Stability Criterion based on the Unified dq-Frame Impedance Network Model for Power Systems with High-Penetration Renewables," *IEEE Trans. Power Syst*., vol. 33, no. 3, pp. 3472-3485, May 2018.

[24] L. Harnefors, X. Wang, A. G. Yepes and F. Blaabjerg, "Passivity-Based Stability Assessment of Grid-Connected VSCs—An Overview," *IEEE J. Emerg. Sel. Topics Power Electron.*, vol. 4, no. 1, pp. 116-125, March 2016.

[25] X. Wang, F. Blaabjerg and P. C. Loh, "Passivity-Based Stability Analysis and Damping Injection for Multiparalleled VSCs with LCL Filters," *IEEE Trans. Power Electron.*, vol. 32, no. 11, pp. 8922-8935, Nov. 2017.

[26] H. Bai, X. Wang, P. C. Loh and F. Blaabjerg, "Passivity Enhancement of Grid-Tied Converters by Series LC-Filtered Active Damper," *IEEE Trans. Ind. Electron.*, vol. 64, no. 1, pp. 369-379, Jan. 2017.

[27] Y. Qiu, M. Xu, K. Yao, J. Sun and F. C. Lee, "Multifrequency Small-Signal Model for Buck and Multiphase Buck Converters," *IEEE Trans. Power Electron.*, vol. 21, no. 5, pp. 1185-1192, Sept. 2006.

[28] J. Sun and K. J. Karimi, "Small-signal input impedance modeling of line-frequency rectifiers," *IEEE Trans. Aerosp. Electron. Syst.*, vol. 44, no. 4, pp. 1489-1497, Oct. 2008.

[29] J. Sun, Z. Bing and K. J. Karimi, "Input Impedance Modeling of Multipulse Rectifiers by Harmonic Linearization," *IEEE Trans. Power Electron.*, vol. 24, no. 12, pp. 2812-2820, Dec. 2009.

2168-6777 (c) 2019 IEEE. Personal use is permitted, but republication/redistribution requires IEEE permission. See http://www.ieee.org/publications_standards/publications/rights/index.html for more information.

This article has been accepted for publication in a future issue of this journal, but has not been fully edited. Content may change prior to final publication. Citation information: DOI 10.1109/JESTPE.2019.2939379, IEEE Journal of Emerging and Selected Topics in Power Electronics

[30] M. Cespedes and J. Sun, "Impedance Modeling and Analysis of Grid-Connected Voltage-Source Converters," *IEEE Trans. Power Electron.*, vol. 29, no. 3, pp. 1254-1261, Mar. 2014.
[31] S. Lissandron, L. Dalla Santa, P. Mattavelli and B. Wen, "Experimental Validation for Impedance-Based Small-Signal Stability Analysis of Single-Phase Interconnected Power Systems With Grid-Feeding Inverters," *IEEE J. Emerg. Sel. Topics Power Electron.*, vol. 4, no. 1, pp. 103-115, Mar. 2016.
[32] J. Sun, "Impedance-Based Stability Criterion for Grid-Connected Inverters," *IEEE Trans. Power Electron.*, vol. 26, no. 11, pp. 3075-3078, Nov. 2011.
[33] X. Feng, J. Liu and F. C. Lee, "Impedance specifications for stable DC distributed power systems," *IEEE Trans. Power Electron.*, vol. 17, no. 2, pp. 157-162, Mar 2002.
[34] S. Vesti, T. Suntio, J. A. Oliver, R. Prieto and J. A. Cobos, "Impedance-Based Stability and Transient-Performance Assessment Applying Maximum Peak Criteria," *IEEE Trans. Power Electron.*, vol. 28, no. 5, pp. 2099-2104, May 2013.
[35] Y. Gu, W. Li and X. He, "Passivity-Based Control of DC Microgrid for Self-Disciplined Stabilization," *IEEE Trans. Power Electron.*, vol. 30, no. 5, pp. 2623-2632, Sept. 2015.
[36] A. Sangwongwanich, Y. Yang and F. Blaabjerg, "High-Performance Constant Power Generation in Grid-Connected PV Systems," *IEEE Trans. Power Electron.*, vol. 31, no. 3, pp. 1822-1825, March 2016.
[37] H. D. Tafti, A. I. Maswood, G. Konstantinou, J. Pou and F. Blaabjerg, "A General Constant Power Generation Algorithm for Photovoltaic Systems," *IEEE Trans. Power Electron.*, vol. 33, no. 5, pp. 4088-4101, May 2018.
[38] A. Keyhani, M. N. Marwali, and M. Dai, *Integration of Green and Renewable Energy in Electric Power Systems*. Hoboken, NJ, USA: Wiley, 2010.
[39] M. G. Villalva, J. R. Gazoli and E. R. Filho, "Comprehensive Approach to Modeling and Simulation of Photovoltaic Arrays," *IEEE Trans. Power Electron.*, vol. 24, no. 5, pp. 1198-1208, May 2009.

Wei Wei received the B.Eng. degree in automation, M.Eng. degree in control theory and control engineering, and D.Eng. degree in power electronics and electronic drives all from the College of Electrical Engineering, Zhejiang University, China, in 1983, 1986 and 1994, respectively. Now he is a professor in the College of Electrical Engineering, Zhejiang University.

His currently research interests includes intelligent control, the development of novel technology of renewable energy and smart grid

Yanghong Xia (S'16-M'19) was born in Hubei Province, China. He received the B.S. degree in automation from the College of Automation, Huazhong University of Science and Technology (HUST), Wuhan, China, and the Ph.D degree in control theory and control engineering from the College of Electrical Engineering, Zhejiang University (ZJU), Hangzhou, China, in 2014 and 2019. Now, he is a Post-doctoral Research Fellow in the joint postdoctoral fellowship program between ZJU and University of Cambridge, Cambridge, U.K..

His current research interests include nonlinear control, distributed generations and microgrid.

Frede Blaabjerg (S'86 - M'88 - SM'97 -F'03) was with ABB-Scandia, Randers, Denmark, from 1987to 1988. From 1988 to 1992, he got the PhD degree in Electrical Engineering at Aalborg University in 1995. He became an Assistant Professor in 1992, an Associate Professor in 1996, and a Full Professor of power electronics and drives in 1998. From 2017 he became a Villum Investigator. He is honoris causa at University Politehnica Timisoara (UPT), Romania and Tallinn Technical University (TTU) in Estonia.

His current research interests includepower electronics and its applications such as in wind turbines, PV systems, reliability, harmonics and adjustable speed drives. He has published more than 600 journal papers in the fields of power electronics and its applications. He is the co-author of four monographs and editor of ten books in power electronics and its applications.

He has received 30 IEEE Prize Paper Awards, the IEEE PELS Distinguished Service Award in 2009, the EPE-PEMC Council Award in 2010, the IEEE William E. Newell Power Electronics Award 2014 and the Villum Kann Rasmussen Research Award 2014. He was the Editor-in-Chief of the IEEE TRANSACTIONS ON POWER ELECTRONICS from 2006 to 2012. He has been Distinguished Lecturer for the IEEE Power Electronics Society from 2005 to 2007 and for the IEEE Industry Applications Society from 2010 to 2011 as well as 2017 to 2018. In 2019-2020, he serves a President of IEEE Power Electronics Society. He is Vice-President of the Danish Academy of Technical Sciences too.

He is nominated in 2014-2018 by Thomson Reuters to be between the most 250 cited researchers in Engineering in the world.

2168-6777 (c) 2019 IEEE. Personal use is permitted, but republication/redistribution requires IEEE permission. See http://www.ieee.org/publications_standards/publications/rights/index.html for more information.